APPLIED SCIENCES AND ENGINEERING

Highly-integrated, miniaturized, stretchable electronic systems based on stacked multilayer network materials

Honglie Song[1,2]†, Guoquan Luo[1,2,3]†, Ziyao Ji[1,2], Renheng Bo[1,2], Zhaoguo Xue[1,2], Dongjia Yan[1,2], Fan Zhang[1,2], Ke Bai[1,2], Jianxing Liu[1,2], Xu Cheng[1,2], Wenbo Pang[1,2], Zhangming Shen[1,2], Yihui Zhang[1,2]*

Elastic stretchability and function density represent two key figures of merits for stretchable inorganic electronics. Various design strategies have been reported to provide both high levels of stretchability and function density, but the function densities are mostly below 80%. While the stacked device layout can overcome this limitation, the soft elastomers used in previous studies could highly restrict the deformation of stretchable interconnects. Here, we introduce stacked multilayer network materials as a general platform to incorporate individual components and stretchable interconnects, without posing any essential constraint to their deformations. Quantitative analyses show a substantial enhancement (e.g., by ~7.5 times) of elastic stretchability of serpentine interconnects as compared to that based on stacked soft elastomers. The proposed strategy allows demonstration of a miniaturized electronic system (11 mm by 10 mm), with a moderate elastic stretchability (~20%) and an unprecedented areal coverage (~110%), which can serve as compass display, somatosensory mouse, and physiological-signal monitor.

INTRODUCTION

Stretchable electronics represent an area of focusing interest in the past decade, in part owing to the broad spectrum of applications, spreading from health monitoring (*1*–*8*) and disease treatment (*9*–*16*), to internet of things (*17*–*20*) and soft robots (*21*–*28*), and to virtual reality and augmented reality (*29*–*34*). Stretchable inorganic electronics mainly rely on integration of high-performance inorganic components with elastomer substrates, where ingenious structural designs are key to a high degree of stretchability of the device system, since inorganic electronic components are usually rigid and brittle (*35*–*42*). For this class of stretchable electronics, the device stretchability and function density [i.e., the areal coverage ratio of individual components (ICs)] represent two crucial performance metrics of the device system, particularly for miniaturized multifunctional systems, noticing the rapidly growing demand of increased complexity of device functionality (*43*–*48*). A higher function density can yield a more miniaturized device system (with a smaller lateral size) than that with a lower function density. While various strategies of stretchable interconnects [e.g., bridge-shaped designs, serpentine interconnects, fractal designs, and helical interconnects (*49*–*55*)] have been developed, the function densities of device systems based on these technologies (mostly in the form of an island-bridge construction) are typically below 80% because of the fundamental limit (100%) of function density for the single-layer layout. These technologies based on the single-layer layout can hardly achieve, simultaneously, a large function density (e.g., >60%) and a sufficient high stretchability (e.g., >20%) for miniaturized multifunctional systems (e.g., consisting of >15 ICs to realize two or more functions) (*51*, *56*–*61*). To bypass the fundamental limit of the single-layer layout, folding-based bilayer layout and stacked multilayer layout were proposed and demonstrated (*51*, *58*, *62*, *63*), which have been used to achieve stretchable systems with a function density of ~76%. These bilayer and multilayer devices exploited soft elastomers (with a modulus from several tens of kilopascals to a few hundreds of kilopascals) to encapsulate serpentine interconnects, but such a solid encapsulation strategy could highly restrict the deformation of serpentine interconnects because of their ultrahigh flexibility, thereby posing a limit to the stretchability of the device system.

Here, we introduce stacked multilayer network materials (SMNMs) as a general framework for integrating and encapsulating inorganic stretchable electronic devices. While the stacked configuration evidently increases the function density of the system, the cellular encapsulation does not pose any essential constraint to the buckled deformation of stretchable interconnects, thereby enabling a substantial enhancement (e.g., by ~7.5 times) of the elastic stretchability as compared to that with solid encapsulation [e.g., using polydimethylsiloxane (PDMS) with a modulus of 0.81 MPa]. Owing to the high air permeability and biomimetic mechanical properties that match nonlinear stress-strain curves of human skin, these multilayer network materials could enhance the comfortableness when laminated on skin (*64*–*69*). Quantitative studies based on finite element analyses (FEA) shed light on the underlying mechanism of constrained deformations of serpentine interconnects encapsulated with network materials and provide rational guidelines for the design optimization. The SMNM-based integration/encapsulation strategy allows the design and demonstration of a millimeter-scale, multifunctional stretchable electronic system (11 mm by 10 mm), with a moderate level (~20%) of elastic stretchability, and, simultaneously, an unprecedented areal coverage (~110%) of ICs. In comparison to previously reported inorganic electronic systems with similar levels of biaxial elastic stretchability and functional complexity (*51*, *53*, *70*), the present system offers a much smaller lateral size (by more than twice) and a much higher areal coverage ratio (110% versus 76%). The device system allows high-precision sensing and wireless radio frequency (RF) transmission of temperature, humidity, and 9–degree-of-freedom motion. Demonstrations in compass display, somatosensory mouse, and real-time monitoring of physiological signals suggest a broad range of application opportunities.

[1]AML, Department of Engineering Mechanics, Tsinghua University, Beijing 100084, P. R. China. [2]Center for Flexible Electronics Technology, Tsinghua University, Beijing 100084, P. R. China. [3]National Key Laboratory of Science and Technology on Advanced Composite in Special Environments, Harbin Institute of Technology, Harbin 150080, P. R. China.
*Corresponding author. Email: yihuizhang@tsinghua.edu.cn
†These authors contributed equally to this work.

RESULTS

Conceptual illustration

Figure 1A presents a schematic illustration of the strategy to integrate and encapsulate stretchable interconnects with soft network materials consisting of periodic triangular lattices of horseshoe microstructures [polyimide (PI); 50 μm in thickness; HD-4110, HD Microsystems]. Here, three serpentine interconnects (3.3-μm PI/0.8-μm Cu/3.3-μm PI) are bonded onto the network material by soldering the three hollow pads (see Materials and Methods and fig. S1 for details of the fabrication process). Apart from the sites of soldering bonding, the other interconnect/network and network/network interfaces are governed by weak van der Waals interactions, such that serpentine interconnects can deform relatively freely under external stretching. Mechanics modeling based on three-dimensional (3D) FEA (see Materials and Methods for details) can well capture the interactions between serpentine interconnects and network materials and predict the constrained deformations of interconnects. Under uniaxial stretching (Fig. 1A, right), the serpentine interconnect, due to the ultrathin feature, tends to undergo lateral buckling that releases the total strain energy through out-of-plane bending and twisting deformations. Although the network layers pose certain constraints at the contact regions with interconnects, the cellular construction allows large out-of-plane deformations, similar to the case (inset of Fig. 1A) of freestanding interconnects without any encapsulation. This mechanism results in a large uniaxial elastic stretchability (~37% in this case), very close to that (46%; fig. S2) of freestanding interconnects. Here, the elastic stretchability denotes the limit of applied strain (ε_{appl}) below which no plastic deformations are induced, such that the structural deformations can recover completely upon unloading.

Figure 1 (B to D) and figs. S3 to S7 provide quantitative results of experiments and FEA that illustrates the advantage of the cellular encapsulation strategy based on bilayer network materials over the conventional solid encapsulation strategy. Here, we choose a widely used encapsulation material (PDMS; with weight ratio of 1:10; elastic modulus, ~0.81 MPa; SYLGARD 184, Dow Corning Corporation) for comparison (*1*, *10*, *15*). In particular, the proposed cellular encapsulation strategy offers a substantially increased elastic stretchability (~45 and 46% according to FEA and experiment, respectively) compared to the case (~6 and 5.3% according to FEA and experiment, respectively) of conventional encapsulation strategy. Such a substantial improvement (by ~7.5 times according to FEA) of elastic stretchability follows from distinct deformation mechanisms induced by the two encapsulation strategies. For the conventional encapsulation strategy, the interconnect is governed mainly by in-plane bending deformations (Fig. 1C) since the out-plane bending and twisting deformations are substantially restricted because of the high flexibility of the PI/Cu/PI interconnect. Here, the dimensions of the PDMS encapsulation are 8.2 mm in length, 2.7 mm in width, and 140 μm in height. Hence, the maximum von Mises stress in the copper layer increases rapidly as the stretching proceeds and reaches the threshold of plastic yielding at ~6%. By contrast, distinct deformation mechanisms can be observed in the case of cellular encapsulation, in which most regions of the serpentine interconnect are suspended, such that the lateral buckling can be easily triggered to form buckled 3D configurations, during the stretching (Fig. 1B). Although the out-of-plane translational motions at regions of the interconnect in contact with network materials are suppressed, their spatial rotations are not limited because of relatively weak van der Waals interactions. Such a weakly constrained deformation mechanism allows a substantial reduction of the von Mises stress in the copper layer, yielding an elastic stretchability of ~45%. This is comparable to the elastic stretchability (~76%) of the same serpentine interconnect in the freestanding condition, i.e., without any mechanical constraints (fig. S3). In the condition of conventional solid encapsulation, the elastic stretchability of the serpentine interconnect increases with decreasing the elastic modulus or the thickness of the encapsulation layer (fig. S8). When the thickness of the PDMS encapsulation reduces from 140 to 60 μm, the resulting elastic stretchability is ~3.8 times lower than that in the case of cellular encapsulation. In comparison to an ultrathin encapsulation (e.g., 100 or 20 μm) with a very soft elastomer (e.g., Ecoflex; 60 kPa) studied previously (*71*), the elastic stretchability with the cellular encapsulation is still ~2.5 times (or ~1.6 times) higher than that of solid encapsulation, in the conditions of 100-μm (or 20-μm) thickness. Note that in the condition of cellular encapsulation, the interface between the interconnect and the network (expect for the bonding region) can be separated easily, for example, at a small applied strain of 15.2%, as shown in fig. S4.

Fatigue tests under cyclic uniaxial stretching (with a fixed strain rate of 6% per second, up to 10,000 cycles) provide quantitative evidence to demonstrate the substantial improvement of elastic stretchability by cellular encapsulation strategy. In particular, the resistance variance of the serpentine interconnect ($\Delta R/R_0$) was measured and averaged after every 500 cycles, as an indicator to identify the fracture of the metal layer. Figure 1D shows that the serpentine interconnect with cellular encapsulation strategy survives 10,000 cycles at a strain amplitude of 45% but fractures after 5500 cycles as the strain amplitude increases to 47% (and after 2000 cycles at the strain amplitude increases to 50%). According to the criterion whether the interconnect can survive 10,000 cycles at a prescribed strain amplitude, the elastic stretchability can be experimentally determined as 46% by averaging these two amplitudes (45 and 47%). In comparison, the serpentine interconnect with conventional encapsulation strategy offers a much lower elastic stretchability (5.3%), according to the experimental measurement (Fig. 1D). Specifically, the interconnect merely endures 5% strain amplitude for 10,000 cycles, and fractures at 5.5% strain amplitude after 9000 cycles. The relative change of the resistance is negligible (<4%) before the interconnect failure. Note that the locations of fatigue fracture observed in experiments are the same as the sites with the maximum von Mises stress in the metal layer of the interconnect, as predicted by FEA for both encapsulation conditions (figs. S5 and S7). In addition to the large elastic stretchability, the serpentine interconnect encapsulated with bilayer network materials also exhibits a J-shaped stress-strain curve under uniaxial stretching (Fig. 1E), which is analogous to that of human skin (fig. S9). The biomimetic mechanical response could enhance the comfortableness when mounted on the skin (figs. S10 and S11). While the cellular encapsulation has a relatively lower restoring force than PDMS encapsulation, the network can deform conformably with the skin and can return to its original shape after unloading because of the highly elastic deformations. In all of the results in Fig. 1 (B to E) and fig. S4, FEA calculations under different encapsulation conditions always agree well with experimental measurements, indicating FEA as a reliable basis of the structural design.

The cellular encapsulation strategy can be extended in a straightforward manner to stacked multilayers of electronic devices, without sacrificing the elastic stretchability. Figure 1 (F and G) presents a five-layer stretchable circuit encapsulated with SMNM, which was

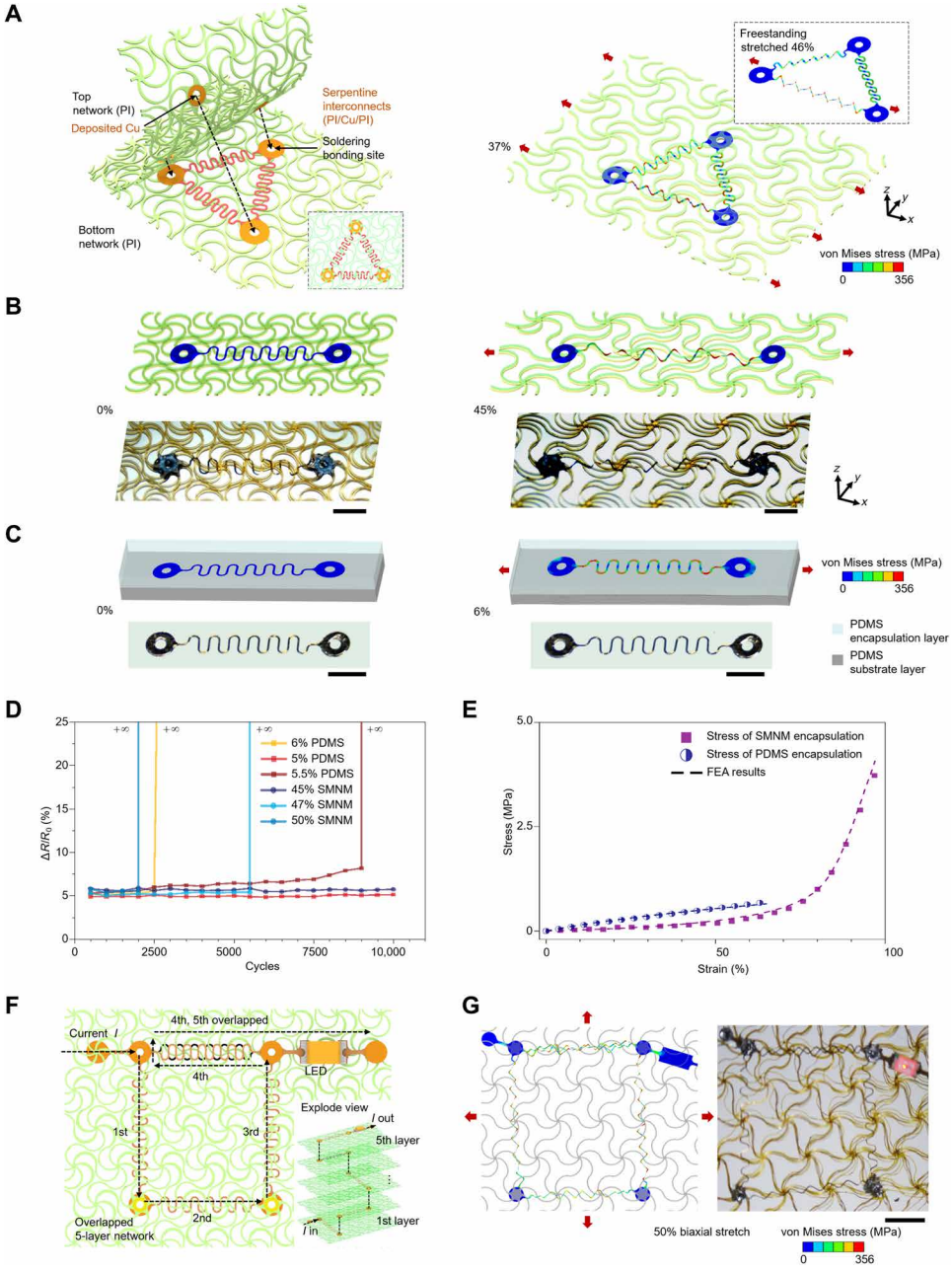

Fig. 1. Conceptual illustration of the combined integration and encapsulation strategy of stretchable interconnects based on SMNMs. (**A**) Process for the integration and encapsulation of serpentine interconnects by a bilayer network material. Right: FEA results for the deformed configuration under 50% uniaxial stretching, in comparison to the case of freestanding serpentine interconnects. The color of serpentine interconnects represents the magnitude of von Mises stress in the metal layer. (**B**) FEA results and optical images of serpentine interconnects encapsulated by a bilayer network material, under 45% uniaxial stretching (corresponding to the elastic stretchability). (**C**) Similar results of serpentine interconnects encapsulated by PDMS solid, under 6% uniaxial stretching. (**D**) Relative variation of the resistance for interconnects encapsulated by PI network and PDMS, under tensile cycling tests with different levels of strain amplitudes. (**E**) Stress-strain curves and associated resistance variations during tensile loading for interconnects encapsulated by PI network and PDMS. (**F**) Design of a stretchable LED device based on the five-layer network material. (**G**) Images and FEA results of the device stretched biaxially to 50%. Scale bars, 1 mm (B, C, and G). Photo credit: H.S., Tsinghua University.

fabricated by transfer printing and stacking of interconnects and network materials through a layer-by-layer process. Each layer of the network material (50 μm in thickness) incorporates a serpentine interconnect (Fig. 1F) and is electrically connected to the neighboring layer through the vertical vias (see fig. S12 for details). The top layer includes a commercial red light-emitting diode (LED) to indicate the on/off state of the entire circuit. Figure 1G shows that the multilayer electronic device maintains a good stability, when biaxially stretched to 50% (corresponding to the elastic stretchability of the device). The deformations of serpentine interconnects at different

layers predicted by FEA are in reasonable agreement with the optical images. Such scalability to multiple stacked layers has important implications in highly integrated, miniaturized stretchable electronics, as to be demonstrated with an example in the section 'Demonstration of miniaturized stretchable electronic system based on SMNM'.

Mechanics of serpentine interconnects with the cellular encapsulation strategy

Quantitative mechanics analyses provide insights into the key design parameters that affect deformation mechanisms of serpentine interconnects with the cellular encapsulation strategy. Figure 2A shows geometric parameters of the serpentine interconnect (with thicknesses of t_{PI} = 3.3 μm and t_m = 0.8 μm) encapsulated with bilayer network materials (with thickness of t_b = 50 μm). The height/spacing ratio L_s/T_s is a key parameter to govern the elastic stretchability of the serpentine interconnect in the freestanding condition (*72*); the length ratio T_s/T_b determines the relative size of the interconnect as compared to the network material, and W_s/T_s is the normalized width of the serpentine interconnect. Since this set of analyses focuses on the constrained deformation of serpentine interconnect, we fix the normalized geometric parameters (normalized width W_b/T_b = 0.0388 and arc angle θ_b = 210°) of the network material for simplicity. Figure 2 (B to E) and figs. S14 and S15 highlight the influences of serpentine designs (L_s/T_s and W_s/T_s) on the deformation mode and elastic stretchability of the interconnect under uniaxial stretching, where the dimension of the network is fixed as T_b = 1.546 mm. For relatively small height/spacing ratios and large normalized widths (e.g., $L_s/T_s < 0.4$ and $W_s/T_s > 0.15$), the stiffness of the serpentine interconnect could be sufficiently high to overcome the constraint of network layers. For example, the buckled deformations of the serpentine interconnect with cellular encapsulation strategy are almost the same as that of freestanding interconnects in the case of L_s/T_s = 0.375 and W_s/T_s = 0.171, according to experimental measurements and FEA calculations (Fig. 2B). As a result, the elastic stretchability (41%) of the encapsulated interconnect is very close to that (47%) of the freestanding interconnect. In comparison, for relatively large height/spacing ratios and small normalized widths (e.g., L_s/T_s = 0.625 and W_s/T_s = 0.171), the serpentine interconnect becomes more flexible, and the deformation of the central region is highly constrained during the external stretching (Fig. 2D, top). Consequently, the serpentine interconnect undergoes a nonuniform unraveling, and the deformations are concentrated at the arc corners close to the two ends. In this case, the elastic stretchability (67%) of the encapsulated interconnect is much smaller than that (92%) of the freestanding interconnect. Figure 2C provides FEA results that depict the dependence of the elastic stretchability on the two design parameters (L_s/T_s and W_s/T_s). Fatigue tests under cyclic uniaxial stretching were performed to determine the elastic stretchabilities for four representative design points (marked as P_1 to P_4 in Fig. 2C). The experimental results (31.3 ± 1.5%, 39.0 ± 1.6%, 31.7 ± 1.5%, and 26.1 ± 2.4% for P_1 to P_4; see figs. S13 and S14 for details) agree reasonably well with the FEA (28, 41, 33, and 27%).

To quantify the constraint effect of the cellular encapsulation on the interconnect, a constraint factor r, defined as $r = \varepsilon_{\text{elastic-stretchability(free)}}/\varepsilon_{\text{elastic-stretchability}}$, is introduced, where $\varepsilon_{\text{elastic-stretchability(free)}}$ is the elastic stretchability in the freestanding condition and $\varepsilon_{\text{elastic-stretchability}}$ is the elastic stretchability with cellular encapsulation. According to this definition, the constraint factor is always larger than 1, and a larger constraint factor suggests a stronger mechanical constraint exerted by the network materials. The contour plot in Fig. 2E shows how the constraint factor is affected by design parameters L_s/T_s and W_s/T_s. As the height/spacing ratio increases or the normalized width decreases, the stiffness of the serpentine interconnect reduces, resulting in an increased constraint factor. As an example, the constraint factor is 1.7 when L_s/T_s = 0.625 and W_s/T_s = 0.114, indicating that the elastic stretchability of encapsulated interconnect is 10/17 of the ideal limit (in the freestanding condition). For parameters that fall in the right, bottom corner, the constraint of the cellular encapsulation is quite weak, such that the elastic stretchability of encapsulated interconnect is very close (e.g., >80% in relative) to the ideal limit. The evident constraint effect of the cellular encapsulation at small normalized widths of W_s/T_s also leads to a nonmonotonic dependence of the elastic stretchability on W_s/T_s (fig. S13), noticing that the elastic stretchability of freestanding serpentine interconnects decreases monotonically with increasing W_s/T_s. Therefore, an optimal normalized width exists (~0.171 in this case), which can maximize the elastic stretchability of serpentine interconnects encapsulated with network materials. In Fig. 2 (A to E), the geometric parameters of the network material are fixed as T_s = 525.2 μm, T_b = 1.546 mm, W_b = 50 μm, t_b = 50 μm, and θ_b = 210°.

Figure 2 (F and G) illustrates the influences of the length ratio T_s/T_b on the elastic stretchability of serpentine interconnects with different height/spacing ratios (L_s/T_s). In this set of analyses, the width (W_s) and spacing (T_s) of the serpentine interconnect are fixed as W_s = 60 μm and T_s = 525.2 μm, with the height/spacing ratio (L_s/T_s) varying from 0.25 to 1, while the network width (W_b) and thickness (t_b) of the network material scale with the node-to-node distance (T_b). The arc angle is fixed as θ_b = 210°. As the relative size (T_s/T_b) of the interconnect becomes smaller, the constraint factor increases because of the enhanced stiffness of the network, thereby inducing a reduction of the elastic stretchability. This is also evidenced by the deformed configurations of the serpentine interconnects (fig. S15). The effect of metal and PI thicknesses on the elastic stretchability and the constraint factor is shown in fig. S16.

Design of SMNM-based stretchable electronic system with unprecedented function density

Harnessing the air-permeable, highly stretchable, and stacked-multilayer configuration, a highly integrated, multifunctional electronic system based on stacked network materials has been demonstrated for personalized health care and complex gesture recognitions. Figure 3A provides a layer-by-layer illustration of the device system, where the circuits and chips are arranged on the first three network layers and the fourth network layer serves for encapsulation. The device system includes 42 ICs and >80 serpentine interconnects (3.3-μm PI/0.8-μm Cu/3.3-μm PI; 60 μm in width) (see figs. S17 to S19 for details). To facilitate the alignment and transfer printing, a customized setup with four-axis manual translation stage (x, y, z, and r) was used (see note S1 for details). Placement of silver pillars into the vertical vias, followed by soldering, connects the neighboring network layers electrically and mechanically. To minimize the vertical dimension of the whole system, certain areas of the network are removed in the first circuit layer, and relatively thick ICs (e.g., motion processing unit and the temperature/humidity sensor) are positioned upside down to penetrate the network layer (Fig. 3A and fig. S17) to further reduce the redundant thickness caused by direct stacking. Note that the thickness (~3.4 mm)

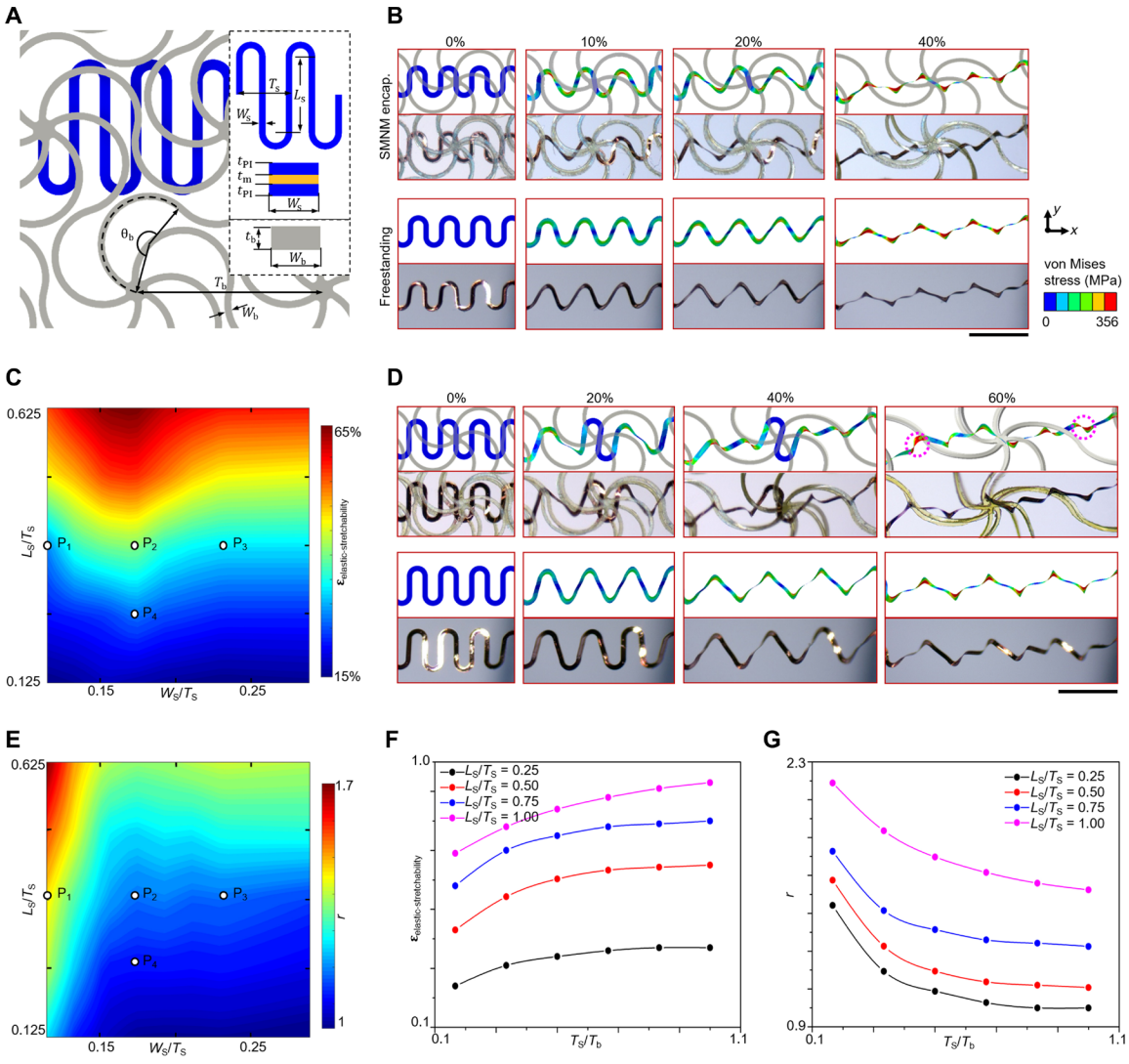

Fig. 2. Experimental and computational studies on the buckling mechanics of stretchable serpentine interconnects encapsulated by two network layers. (**A**) Illustration of key geometric parameters for a serpentine interconnect encapsulated by two network layers. (**B**) Optical images and corresponding FEA results on deformation sequences of a serpentine interconnect [$W_s/T_s = 0.171$ and $L_s/T_s = 0.375$; marked as P_2 in (C)] encapsulated by network materials, in comparison to that in the freestanding condition. (**C**) Contour plot of the interconnect elastic stretchability ($\varepsilon_{elastic\text{-}stretchability}$) in terms of the design parameters W_s/T_s and L_s/T_s. The design parameters (W_s/T_s, L_s/T_s) of the five design points (P_1 to P_5) are (0.114, 0.375), (0.171, 0.375), (0.228, 0.375), (0.171, 0.250), and (0.171, 0.625), respectively. (**D**) Optical images and corresponding FEA results on deformation sequences of a serpentine interconnect [$W_s/T_s = 0.171$ and $L_s/T_s = 0.625$; marked as P_5 in (C)] encapsulated by network materials. (**E**) Contour plot of the constraint factor (r) in terms of design parameters W_s/T_s and L_s/T_s. (**F**) Interconnect elastic stretchability versus the design parameter T_s/T_b for a range of different height/spacing ratios (L_s/T_s). (**G**) Constraint factor versus the design parameter T_s/T_b for a range of different height/spacing ratios (L_s/T_s). Photo credit: H.S., Tsinghua University.

of the entire system can be further reduced by grinding the excessive packaging epoxy of the chips away (*51*, *63*). The resulting device system has a lateral dimension (11 mm by 10 mm) comparable to that of the fingertip (Fig. 3B, top). Despite a relatively large thickness (~3.4 mm) of the system as compared to the epidermal electronics reported previously (*51*, *53*, *73*–*76*), the stacked layout does not cause an accumulation of the bending stress in the serpentine interconnect. Therefore, the entire system can be conformally attached onto a rigid glass rod with 3 mm in radius (Fig. 3B, bottom), showing an excellent bendability of the device system. In addition, the device system can survive other levels of deformations, such as pressing (~15%), out-of-plane shearing (~30°), and twisting (attached on an Ecoflex film and twisted by ~540°), suggesting an excellent robustness of the multilayered device system (fig. S20). Moreover, sealing the connection vias of all circuit layers with dielectric elastomers {e.g., silicone rubber [706, room temperature vulcanized silicone rubber (RTV), NanDa]} can enhance the water resistance of the device system (fig. S21). To further enhance the robustness of multilayer device systems, denser network could be exploited to serve as the top encapsulation layer, and the edge of the device can be encapsulated with soft elastomers (fig. S22).

Stretchability and function density (i.e., areal coverage) are key figures of merits of flexible electronic systems. To allow a clear understanding of the system-level deformations, both mechanics

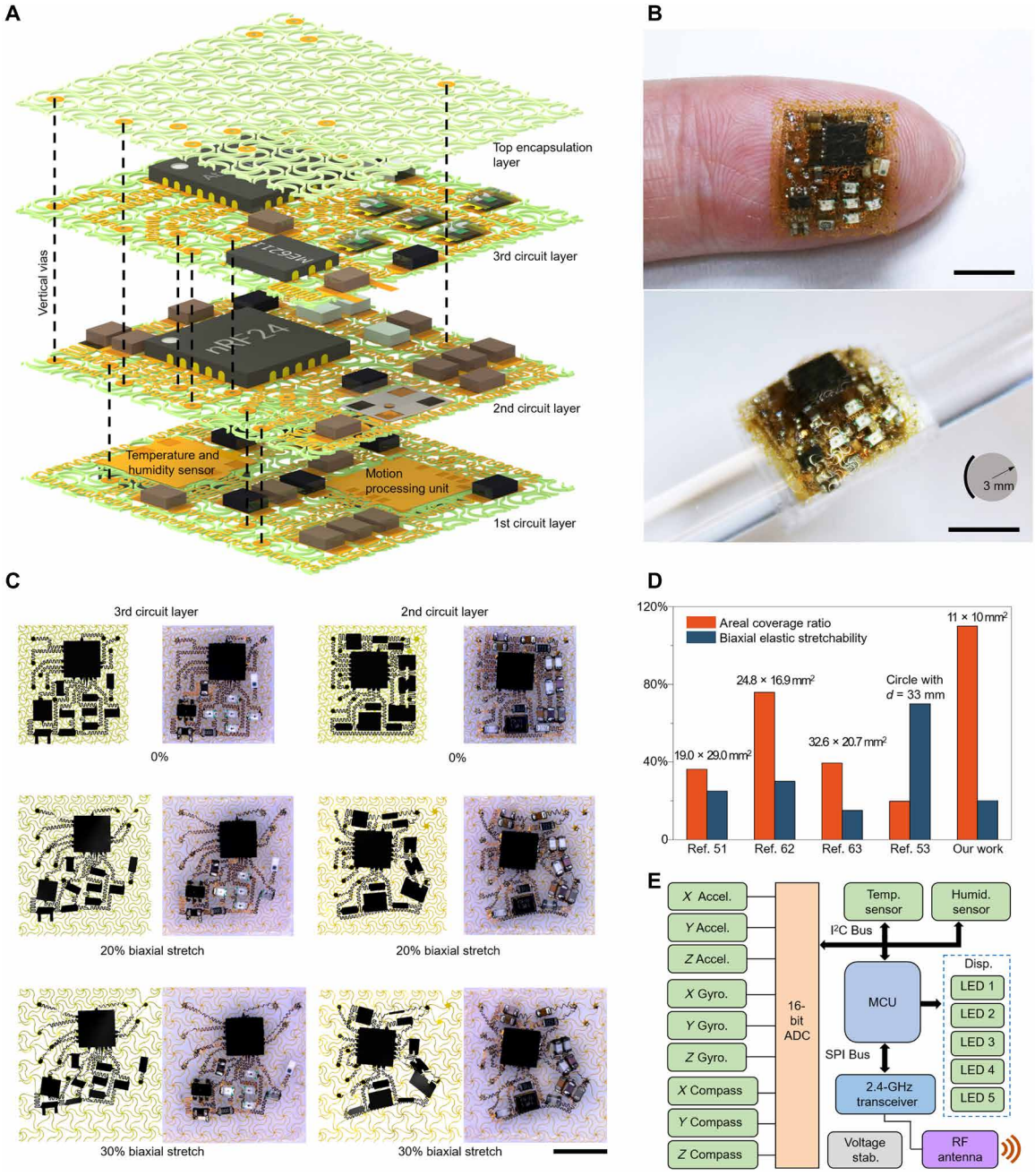

Fig. 3. Design and fabrication of densely packed, stretchable electronic system based on SMNM. (**A**) Schematic illustration of the device system in an exploded view. The system contains 42 ICs, with lateral dimensions of ~11.2 mm by 10.1 mm and an areal coverage ratio of ~110%. Subcircuits are aligned and electrically connected through vertical vias, highlighted by dashed lines. (**B**) Photographs of the SMNM-based stretchable electronic system mounted on an index finger (top) and wrapped around a glass rod (bottom). (**C**) System-level deformations determined by FEA and experimental photographs for the top and middle circuit layers, during different levels of biaxial stretching (0, 20, and 30%). (**D**) Areal coverage ratio versus elastic stretchability for various stretchable skin-integrated electronic devices, including the current work and those reported previously. (**E**) Block diagrams of the functional components for physiological tracking, including monitoring of human motion, temperature, and humidity. The system mainly consists of a nine-axis MEMS motion-processing unit (MPU-9250; including three-axis gyroscope, three-axis accelerometer, and three-axis magnetometer), a digital high-accuracy temperature and humidity sensor (HTU21D), a microcontroller unit (Atmega328P), 2.4-GHz RF wireless transceivers (nRF24L), and five LEDs. Scale bars, 5 mm (B and C). Photo credit: H.S., Tsinghua University.

simulations and biaxial tensile tests have been carried out for each circuit layer. Figure 3C illustrates the structural evolutions of two representative layers (second and third layers) under 30% biaxial stretching. The trivial bending/twisting deformations and translational/rotational motions of various interconnects in the circuit are well captured by FEA. Quantitative calculations show that both of these two circuits can withstand a biaxial stretching of 30%, in a reversible manner (figs. S23 and S24). The serpentine interconnects and ICs

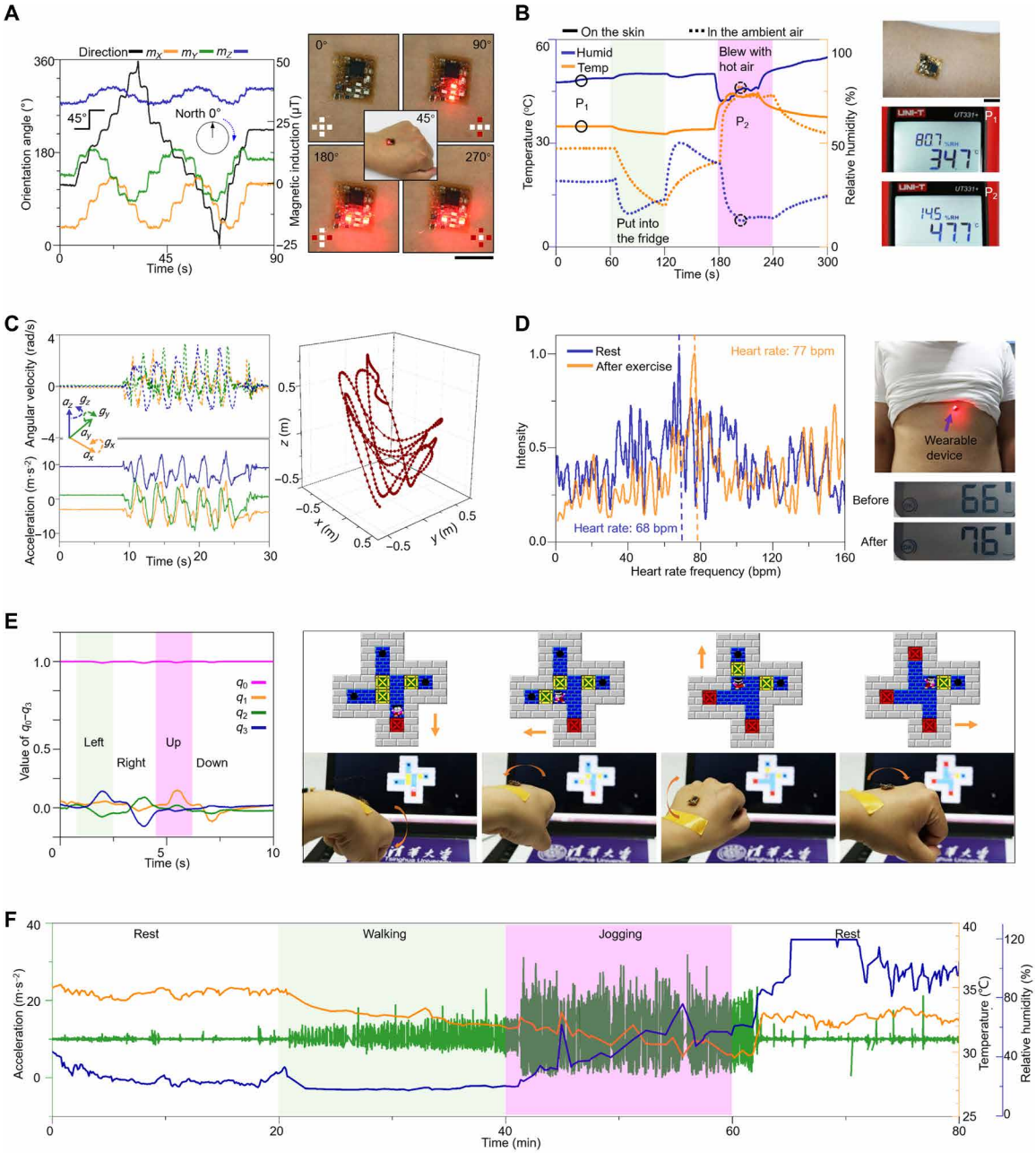

Fig. 4. Demonstration of functional characteristics of the SMNM-based electronic system. (**A**) Left: Recorded data of three-axis magnetic induction. Right: Device mounted on the hand to serve as a compass display. Scale bar, 10 mm. (**B**) Left: Results of the temperature and relative humidity. Right: The device mounted on the arm and images of temperature and relative humidity results from a commercial meter. (**C**) Left: Representative recordings of three-axis acceleration and three-axis angular velocity from the palm. Right: Reconfigured 3D motion curves. (**D**) Left: Results of heart rates extracted from the frequency analysis of accelerometer data, obtained from the device placed on the chest. Right: Device mounted on the chest and heart rates measured with a commercial sphygmomanometer. (**E**) Proof-of-concept demonstration of a wireless mouse application. Left: Raw signals of quaternions (q_0, q_1, q_2, and q_3) obtained from the device are processed to yield representative vital signs for gesture recognition. Right: Photographs showing the control of the Sokoban pushing box game through hand gesture (i.e., move up, down, left, and right) recognition. (**F**) Physiological monitoring of the acceleration, temperature, and relative humidity of the body epidermis while going through a cycle (80 min) of rest-walking-jogging-rest. Photo credit: H.S., Tsinghua University.

do not contact each other throughout the deformation process (fig. S24). The entire device system offers a moderate level of elastic stretchability (~20%). After fifty cycles of uniaxial stretching (10%) and releasing when mounted on skin, the out-of-plane deformations of serpentine interconnects are restored, and no interconnects are stuck on the skin (fig. S25). In addition, the rational design of the planar arrangement of ICs in each layer enables 110% areal coverage of the multilayer system, inaccessible through the single-layer layout. Compared with the device system encapsulated with multilayer solid elastomers, the design of interconnect layout in the case of

SMNM encapsulation is more flexible because of the lower mechanical constraints of SMNM encapsulation to the interconnect deformation, which is beneficial to the enhancement of both the areal coverage ratio and the elastic stretchability. Figure 3D shows that this value (110%) is much larger than that (up to 76%) of representative stretchable inorganic electronic systems with similar levels of functional complexity previously reported (*51*, *53*, *62*, *63*). The high degree of functional integration also allows highly miniaturized device system (fig. S26), as evidenced by the lateral size (11 mm by 10 mm) that is much smaller (by more than twice) than those reported previously (*51*, *53*, *62*, *63*). Note that the function density of our device system can be further increased by increasing the number of layers, although the total thickness could be a limiting factor. Thermal measurements showed that the temperature of the device system increases very slightly after working for several minutes, which can be partially attributed to the enhanced thermal convection due to the cellular microstructures (fig. S27).

Figure 3E presents the modular design of the multilayer electronic system affording wireless monitoring of complex motions, geomagnetic inductions, temperature, and relative humidity (see Materials and Methods and figs. S28 to S30 for details). The obtained raw data of motions and geomagnetic inductions were converted into digital signals via 16-bit analog-to-digital converters (ADCs). These converted signals and the acquired temperature/humidity data were sent through the I^2C bus to the microcontrol unit for processing. The outputs were then used to control the on/off states of the five LEDs. Meanwhile, the filtered signals were transmitted wirelessly to the host computer via RF protocol. A customized program based on the software MATLAB was used for data logging and advanced human interface applications.

Demonstration of miniaturized stretchable electronic system based on SMNM

Figure 4 demonstrates a range of applications of the highly integrated, miniaturized, multifunctional electronic system. The measured components (m_x, m_y, and m_z) of the geomagnetic induction can be used to determine its orientation angle [Fig. 4A (left) and fig. S31]. The device can thereby serve as a compass to display the orientation angle by exploiting different lighting modes of the LED array (on the third circuit layer) to denote different ranges of the angle [Fig. 4A (right) and fig. S32]. For example, all of the five LEDs are off when the orientation angle is in the range of 0° and 45°, and only the top and bottom LEDs are on when the orientation angle is in the range of 90° and 135°. Figure 4B shows the time-varying temperature and relative humidity at the skin surface when mounted on the arm. The device was put into a fridge from 60 to 120 s and blew with hot air from 180 to 240 s. The results (34.9°C and 80.8% at 30 s; 46.3°C and 14.1% at 200 s) measured through the stretchable device are consistent with the data (34.7°C and 80.7% at 30 s; 47.7°C and 14.5% at 200 s) acquired from the commercial sensor (UT331+, Uni-Trend Technology) (Fig. 4B, right). Monitoring of motion signals (Fig. 4C, left), including components of the acceleration (a_x, a_y, a_z) and angular velocity (g_x, g_y, g_z), allows reconfiguration of the 3D motion trajectory [Fig. 4C (right) and movie S3] and tracking of the heart rate (Fig. 4D). The measured heart rates are close to those measured by a commercial sphygmomanometer (U12, Omron) before and after exercise (fig. S33). Figure 4E (left) presents the utility of the motion signals (collected through the three-axis gyroscope) as a means to identify the hand gesture (i.e., move left, right, top, and bottom). This enables a demonstrative application of somatosensory mouse (mounted on the back of the hand) to complete a "Sokoban pushing box" game [Fig. 4E (right) and movie S4]. Owing to the high air permeability and biomimetic mechanical properties that match those of human skin, the SMNM-based, miniaturized, stretchable device system could enhance the comfortableness of skin integration and is thereby particularly suitable for long-term monitoring of physiological signals. Figure 4F provides an 80-min monitoring of the acceleration, temperature, and relative humidity, with the device mounted on the chest, during a cycle of rest, walking, jogging, and rest.

DISCUSSION

Collectively, this work presents strategic designs and mechanics analyses that establish SMNMs as a synergistic platform to integrate and encapsulate inorganic stretchable electronic devices. The SMNM-based platform not only offers a significantly enhanced (e.g., by 7.5 times) elastic stretchability of serpentine interconnect by relieving the mechanical constraint but also provides a scalable route to increased function density by exploiting more stacking layers. A highly integrated, miniaturized, stretchable device system with ultrahigh areal coverage (~110%) and small size (11 mm by 10 mm) is demonstrated, with capabilities in compass display, somatosensory mouse control, and physiological signal monitor. The proposed design strategies based on the SMNM have general utilities in various types of electronic devices, especially those (e.g., virtual reality devices and human-machine interfaces) that demand high levels of function density. Development of SMNM-based electronic devices with complex 3D shapes (e.g., tubes and hemispheres) to allow conformal integration with biological organs (e.g., vessels and nerve guide conduits) represents a promising direction for future work.

MATERIALS AND METHODS

Finite element analysis

The commercial software ABAQUS was used to predict the constrained deformations and calculate the elastic stretchability of the serpentine interconnect encapsulated by SMNM. We adopted four-node 2D shell elements (S4R) with three-layer laminates of PI/Cu/PI to model the serpentine interconnect and eight-node 3D solid elements (C3D8R) to model the multilayer network. An explicit solver was adopted to ensure the convergence of the simulations that involve complex contact interactions between serpentine interconnect and multilayer network. An ideal elastic-plastic constitutive model was used for copper, with an elastic modulus of 119 GPa, a Poisson's ratio of 0.34, and a yield strength of 356 MPa (corresponding to ~0.3% yield strain). The elastic stretchability corresponds to the applied strain at which the von Mises stress of the metal layer at the top or bottom surface reach the yield strength across the width of any section of the serpentine interconnect. This criterion has been verified by experimental measurements and adopted in many previous studies (*52*, *53*). A typical hyperelastic constitutive relation (i.e., the Mooney-Rivlin law) captured mechanical properties of the elastomer (PDMS) used for solid encapsulation (elastic modulus E_{PDMS} = 0.81 MPa and Poisson's ratio ν_{PDMS} = 0.49) (fig. S34). The elastic modulus E and Poisson's ratio ν of PI are E_{PI} = 1.9 GPa and ν_{PI} = 0.27 (fig. S35). A hard and frictionless contact was adopted for the contact regions between the network and the serpentine interconnects, except for the bonding regions, where a "tie" constraint (in ABAQUS) was exploited. Fixed displacement boundary

conditions were applied to the four sides of the network specimen. For uniaxial loading, the displacement components were set as ($u_x = 0$, $u_z = 0$) for the left side and ($u_x = \varepsilon_{appl}L_x$, $u_z = 0$) for the right side, where L_x is the length of the network specimen along the x direction. For biaxial loading, the displacement components were set as ($u_x = 0$, $u_z = 0$), ($u_x = \varepsilon_{appl}L_x$, $u_z = 0$), ($u_y = 0$, $u_z = 0$), and ($u_y = \varepsilon_{appl}L_y$, $u_z = 0$) for the left, right, down, and up sides, respectively, where L_y is the length of the network specimen along the y direction.

Fabrication of the stretchable serpentine interconnects for mechanical testing

Spin-casting the poly(methyl methacrylate) (PMMA; ~150 nm in thickness; MicroChem, USA), and baking (15 mins at 180°C) formed a sacrificial thin layer on a silicon wafer. Spin-casting PI (~3.3 μm in thickness; HD Microsystems, USA), thermal curing (2 hours at 250°C), followed by depositing metal layers (Cu, thickness of 0.8 μm) by electron beam evaporation, photolithography processing, wet-etching, spin-casting another PI (~3.3 μm in thickness), and thermal curing formed the PI/Cu/PI film. Oxygen reactive ion etching by depositing another metal layer (Ti, thickness ~ 40 nm) to serve as the mask defined the PI/Cu/PI serpentine interconnects. Immersing the silicon into acetone to dissolve the PMMA and retrieval of the PI/Cu/PI interconnects onto a PDMS (SYLGARD 184, Dow Corning Corporation, USA) stamp allowed delivery to another substrate via transfer printing, as illustrated in fig. S36. The thickness of PI layers was measured by a stylus profiler (Bruker, Dektak XT).

Fabrication of a bilayer PI network for encapsulation of serpentine interconnects

Spin-casting the PMMA (~150 nm) and baking (15 min at 180°C) on a silicon wafer, then spin-casting photo-definable PI (50 μm), followed by photolithographic patterning and curing yielded a PI network with horseshoe microstructures. Selective deposition of Cu layer (0.8 μm) by electron beam evaporation through a shadow mask, defined sites for soldering to form vias. Immersing the silicon wafer in acetone allowed the retrieval of the PI network. Transfer printing the PI network layer onto a PDMS substrate, delivering serpentine interconnects onto PDMS@glass slide, and then placing the two glass slides on a customized mechanical stage (i.e., a four-axis manual translation stage, x, y, z, and r, with travel accuracy of 1 μm for x, y, and z stages and minimal readable resolution of ~0.015° for r stage) allowed precisely controlled alignment and soldering (figs. S36 to S39). A conductive alloy ($In_{97}Ag_3$) served as the material for soldering and established electrical connections between ICs and serpentine interconnects. Transfer printing another layer of PI network and repeating the aforementioned alignment and soldering procedures completed the fabrication of a bilayer PI network with an encapsulated serpentine interconnect.

Cyclic stretching test of serpentine interconnects encapsulated by bilayer network materials or soft elastomers

A customized uniaxial mechanical stretcher allowed precisely controlled levels of strains to the interconnects encapsulated by stacked bilayer network materials or solidified PDMS, at a strain rate (6% per second, for 10,000 cycles). Three to five sets of repeated cycling tests were conducted to ensure consistency. A charge-coupled device camera with 10× lens (Navitar Zoom 6000 Lens System, USA) and a digital multimeter (Keysight 34465A, USA) allowed recording of the deformation and resistance of the encapsulated serpentine interconnects at different numbers of cycles.

Circuit design and fabrication of the multifunctional stretchable electronic system

A nine-axis micro-electro-mechanical system (MEMS) motion-processing unit (MPU-9250, TDK Corporation) enabled measurements from the three-axis gyroscope, three-axis accelerometer, and three-axis magnetometer. The configuration step involved nine 16-bit ADCs for digitizing outputs, over a range of ±2000°/s for the gyroscope, ±16 g for the accelerometer, and ±4800 μT for the magnetometer. A digital high-accuracy relative humidity and temperature sensor (HTU21D, Humirel) offered 14-bit digital outputs for humidity ranging from 0 to 100% ± 5% and temperature ranging from −40° to 125° ± 0.5°C through I^2C bus. An 8-bit microcontroller (Atmega328P, Atmel) served as the onboard signal processing unit. It collected signals with a Kalman filter and then controlled the lighting mode of the LED array. The processed digital signal was sent to a 2.4-GHz transceiver (nRF24L01, Nordic Semiconductor) through a serial peripheral interface bus and then wirelessly transmitted to the user interface. Five LEDs used to display the state of the compass were divided into three groups, where LED1-LED2, LED3, and LED4-LED5 were connected to pin 20, pin 21, and pin 19 of the microcontroller, respectively. The voltage stabilizing module mainly consisted of a high-speed low-dropout regulator (ME6211, Nanjing Micro One Electronics Inc.).

In the electronic system, short silver pillars (~0.1 mm in diameter) cross the vias of each PI network to connect the subcircuits at different layers. Soldering the silver pillars at the vias of each network layer ensures mechanical and electrical robustness of vertical connections. In the first circuit layer, the MPU-9250 was placed on the opposite side of serpentine interconnects to attain a reduced total thickness (~3.4 mm) of the entire device system.

Programming the wireless embedded system

The commercial packages including Keil μVision and a 2.4-GHz transceiver (nRF24L01, Nordic Semiconductor) served as tools for building software for the device system. Wireless transmission of outputs from the stretchable electronics occurred in data packets with sizes of 12 bytes. A custom Arduino-based circuit board receives the signals and then sends the packages to the laptop via COM ports. The software MATLAB is used to define the graphical user interface with the function of data logging for further signal processing.

Measurement of motion and physiological signals

The integrated system of the multilayer electronic device and a Li battery that serves as the power supply was adhered to the arm and chest to collect motion and physiological signals. Waving the arm to form a number "8" shape in space, the reconfigured 3D motion curves (Fig. 4) were obtained by the host computer with a custom MATLAB interface based on the signals of acceleration and angular velocity. For the sensing of temperature and relative humidity, a commercial temperature humidity meter (UT331+, Uni-Trend Technology, China) served as a reference for comparison. For the monitoring of heart rates, a commercial household sphygmomanometer (U12, Omron) was used for comparison. With the integrated system mounted on the chest, the heart rate was determined by sampling the three-axis acceleration and processing the data by Fourier transform. The

physiological signals, including the relative humidity, temperature, and heart rate over a long period (80 min) of motion, were measured (Fig. 4F).

Demonstration of the compass display

The three-axis magnetometer in MPU-9250 unit allowed calculation of the orientation angle, which was used to control the display mode of the LED array, according to the coding rules detailed in fig. S26.

Demonstration of the somatosensory mouse

The RF wireless module in the integrated system sent signals of three-axis angular velocity (g_x, g_y, g_z) to the receiving module connected to the laptop via COM ports. The resolutions of the accelerometer and the gyroscope were about 244 μg (over a range of ±16 g) and ±0.031°/s, which can ensure an accurate motion capture. The captured motion allowed the direction control of the mouse to perform the Sokoban pushing box game, where the pushing direction (up, down, left, and right) was controlled by the rotation of the palm.

Protocols for human subject studies

The studies about the human subjects were approved by the Institutional Review Board of Tsinghua University (no. 20220008). Volunteers without skin lesions were recruited and joined the studies after understanding the contents of the study and signing consent forms. For the demonstrations of the compass, temperature/humidity measurements of the skin surface, 3D motion trajectory, and the somatosensory mouse, the device was attached to the back of the hand or arms. For the demonstrations of the heart-rate monitoring, the device was mounted on the chest with a silicone-based surgical tape (Kind Removal Silicone Tape, 3M Inc., USA). All subjects consented to their images being taken as detailed in the protocols of the Institutional Review Board of Tsinghua University.

SUPPLEMENTARY MATERIALS

Supplementary material for this article is available at https://science.org/doi/10.1126/sciadv.abm3785

REFERENCES AND NOTES

1. Y. Wang, S. Lee, T. Yokota, H. Wang, Z. Jiang, J. Wang, M. Koizumi, T. Someya, A durable nanomesh on-skin strain gauge for natural skin motion monitoring with minimum mechanical constraints. *Sci. Adv.* **6**, eabb7043 (2020).
2. S.-H. Sunwoo, K.-H. Ha, S. Lee, N. Lu, D.-H. Kim, Wearable and implantable soft bioelectronics: Device designs and material strategies. *Annu. Rev. Chem. Biomol. Eng.* **12**, 359–391 (2021).
3. C. Lim, Y. J. Hong, J. Jung, Y. Shin, S.-H. Sunwoo, S. Baik, O. K. Park, S. H. Choi, T. Hyeon, J. H. Kim, S. Lee, D.-H. Kim, Tissue-like skin-device interface for wearable bioelectronics by using ultrasoft, mass-permeable, and low-impedance hydrogels. *Sci. Adv.* **7**, eabd3716 (2021).
4. C. Peng, M. Chen, H. K. Sim, Y. Zhu, X. Jiang, Noninvasive and nonocclusive blood pressure monitoring via a flexible piezo-composite ultrasonic sensor. *IEEE Sens. J.* **21**, 2642–2650 (2021).
5. W. Zhou, S. Yao, H. Wang, Q. Du, Y. Ma, Y. Zhu, Gas-permeable, ultrathin, stretchable epidermal electronics with porous electrodes. *ACS Nano* **14**, 5798–5805 (2020).
6. Z. Zou, C. Zhu, Y. Li, X. Lei, W. Zhang, J. Xiao, Rehealable, fully recyclable, and malleable electronic skin enabled by dynamic covalent thermoset nanocomposite. *Sci. Adv.* **4**, eaaq0508 (2018).
7. H. Guo, Y. J. Tan, G. Chen, Z. Wang, G. J. Susanto, H. H. See, Z. Yang, Z. W. Lim, L. Yang, B. C. K. Tee, Artificially innervated self-healing foams as synthetic piezo-impedance sensor skins. *Nat. Commun.* **11**, 5747 (2020).
8. Y. Yang, K. Xu, T. Vervust, J. Vanfleteren, Multifunctional and miniaturized flexible sensor patch: Design and application for in situ monitoring of epoxy polymerization. *Sens. Actuators B* **261**, 144–152 (2018).
9. H. Sheng, J. Zhou, B. Li, Y. He, X. Zhang, J. Liang, J. Zhou, Q. Su, E. Xie, W. Lan, K. Wang, C. Yu, A thin, deformable, high-performance supercapacitor implant that can be biodegraded and bioabsorbed within an animal body. *Sci. Adv.* **7**, eabe3097 (2021).
10. H. Joo, Y. Lee, J. Kim, J.-S. Yoo, S. Yoo, S. Kim, A. K. Arya, S. Kim, S. H. Choi, N. Lu, H. S. Lee, S. Kim, S.-T. Lee, D.-H. Kim, Soft implantable drug delivery device integrated wirelessly with wearable devices to treat fatal seizures. *Sci. Adv.* **7**, eabd4639 (2021).
11. Y. Gao, L. Yu, J. C. Yeo, C. T. Lim, Flexible hybrid sensors for health monitoring: Materials and mechanisms to render wearability. *Adv. Mater.* **32**, 1902133 (2020).
12. B. Kim, A. H. Soepriatna, W. Park, H. Moon, A. Cox, J. Zhao, N. S. Gupta, C. H. Park, K. Kim, Y. Jeon, H. Jang, D. R. Kim, H. Lee, K.-S. Lee, C. J. Goergen, C. H. Lee, Rapid custom prototyping of soft poroelastic biosensor for simultaneous epicardial recording and imaging. *Nat. Commun.* **12**, 3710 (2021).
13. K. Kim, H. J. Kim, H. Zhang, W. Park, D. Meyer, M. K. Kim, B. Kim, H. Park, B. Xu, P. Kollbaum, B. W. Boudouris, C. H. Lee, All-printed stretchable corneal sensor on soft contact lenses for noninvasive and painless ocular electrodiagnosis. *Nat. Commun.* **12**, 1544 (2021).
14. E. K. Lee, R. K. Baruah, J. W. Leem, W. Park, B. H. Kim, A. Urbas, Z. Ku, Y. L. Kim, M. A. Alam, C. H. Lee, Fractal web design of a hemispherical photodetector array with organic-dye-sensitized graphene hybrid composites. *Adv. Mater.* **32**, 2004456 (2020).
15. J. Koo, S. B. Kim, Y. S. Choi, Z. Xie, A. J. Bandodkar, J. Khalifeh, Y. Yan, H. Kim, M. K. Pezhouh, K. Doty, G. Lee, Y.-Y. Chen, S. M. Lee, D. D'Andrea, K. Jung, K. Lee, K. Li, S. Jo, H. Wang, J.-H. Kim, J. Kim, S.-G. Choi, W. J. Jang, Y. S. Oh, I. Park, S. S. Kwak, J.-H. Park, D. Hong, X. Feng, C.-H. Lee, A. Banks, C. Leal, H. M. Lee, Y. Huang, C. K. Franz, W. Z. Ray, M. MacEwan, S.-K. Kang, J. A. Rogers, Wirelessly controlled, bioresorbable drug delivery device with active valves that exploit electrochemically triggered crevice corrosion. *Sci. Adv.* **6**, eabb1093 (2020).
16. H. Kim, Y.-T. Kwon, C. Zhu, F. Wu, S. Kwon, W.-H. Yeo, H. J. Choo, Real-time functional assay of volumetric muscle loss injured mouse masseter muscles via nanomembrane electronics. *Adv. Sci.* **8**, 2101037 (2021).
17. K. Bai, X. Cheng, Z. Xue, H. Song, L. Sang, F. Zhang, F. Liu, X. Luo, W. Huang, Y. Huang, Y. Zhang, Geometrically reconfigurable 3D mesostructures and electromagnetic devices through a rational bottom-up design strategy. *Sci. Adv.* **6**, eabb7417 (2020).
18. M. Wang, Z. Yan, T. Wang, P. Cai, S. Gao, Y. Zeng, C. Wan, H. Wang, L. Pan, J. Yu, S. Pan, K. He, J. Lu, X. Chen, Gesture recognition using a bioinspired learning architecture that integrates visual data with somatosensory data from stretchable sensors. *Nat. Electron.* **3**, 563–570 (2020).
19. Z. Cui, W. Wang, L. Guo, Z. Liu, P. Cai, Y. Cui, T. Wang, C. Wang, M. Zhu, Y. Zhou, W. Liu, Y. Zheng, G. Deng, C. Xu, X. Chen, Haptically quantifying Young's modulus of soft materials using a self-locked stretchable strain sensor. *Adv. Mater.* **8**, 2104078 (2021).
20. Y. Wang, L. Yin, Y. Bai, S. Liu, L. Wang, Y. Zhou, C. Hou, Z. Yang, H. Wu, J. Ma, Y. Shen, P. Deng, S. Zhang, T. Duan, Z. Li, J. Ren, L. Xiao, Z. Yin, N. Lu, Y. Huang, Electrically compensated, tattoo-like electrodes for epidermal electrophysiology at scale. *Sci. Adv.* **6**, eabd0996 (2020).
21. W. Li, N. Matsuhisa, Z. Liu, M. Wang, Y. Luo, P. Cai, G. Chen, F. Zhang, C. Li, Z. Liu, Z. Lv, W. Zhang, X. Chen, An on-demand plant-based actuator created using conformable electrodes. *Nat. Electron.* **4**, 134–142 (2021).
22. L. Beker, N. Matsuhisa, I. You, S. R. A. Ruth, S. Niu, A. Foudeh, J. B. H. Tok, X. Chen, Z. Bao, A bioinspired stretchable membrane-based compliance sensor. *Proc. Natl. Acad. Sci.* **117**, 11314–11320 (2020).
23. D. Jung, C. Lim, J. Shim Hyung, Y. Kim, C. Park, J. Jung, I. Han Sang, S.-H. Sunwoo, W. Cho Kyoung, D. Cha Gi, C. Kim Dong, H. Koo Ja, H. Kim Ji, T. Hyeon, D.-H. Kim, Highly conductive and elastic nanomembrane for skin electronics. *Science* **373**, 1022–1026 (2021).
24. P. Ren, Y. Liu, R. Song, B. O'Connor, J. Dong, Y. Zhu, Achieving high-resolution electrohydrodynamic printing of nanowires on elastomeric substrates through surface modification. *ACS Appl. Electron. Mater.* **3**, 192–202 (2021).
25. R. Song, S. Yao, Y. Liu, H. Wang, J. Dong, Y. Zhu, B. T. O'Connor, Facile approach to fabricating stretchable organic transistors with laser-patterned Ag nanowire electrodes. *ACS Appl. Mater. Interfaces* **12**, 50675–50683 (2020).
26. K. Sim, Z. Rao, Z. Zou, F. Ershad, J. Lei, A. Thukral, J. Chen, Q.-A. Huang, J. Xiao, C. Yu, Metal oxide semiconductor nanomembrane based soft unnoticeable multifunctional electronics for wearable human-machine interfaces. *Sci. Adv.* **5**, eaav9653 (2019).
27. R. H. Soon, L. Yu, C. T. Lim, A soft sensorized microfluidic tubular actuating gripper. *Adv. Mater. Technol.* **5**, 2000150 (2020).
28. C. Linghu, S. Zhang, C. Wang, K. Yu, C. Li, Y. Zeng, H. Zhu, X. Jin, Z. You, J. Song, Universal SMP gripper with massive and selective capabilities for multiscaled, arbitrarily shaped objects. *Sci. Adv.* **6**, eaay5120 (2020).
29. M. Nasreldin, S. de Mulatier, R. Delattre, M. Ramuz, T. Djenizian, Flexible and stretchable microbatteries for wearable technologies. *Adv. Mater. Technol.* **5**, 2000412 (2020).
30. P. Cai, C. Wan, L. Pan, N. Matsuhisa, K. He, Z. Cui, W. Zhang, C. Li, J. Wang, J. Yu, M. Wang, Y. Jiang, G. Chen, X. Chen, Locally coupled electromechanical interfaces based on cytoadhesion-inspired hybrids to identify muscular excitation-contraction signatures. *Nat. Commun.* **11**, 2183 (2020).
31. S. Lee, S. Franklin, A. Hassani Faezeh, T. Yokota, M. G. Nayeem, Y. Wang, R. Leib, G. Cheng, D. W. Franklin, T. Someya, Nanomesh pressure sensor for monitoring finger manipulation without sensory interference. *Science* **370**, 966–970 (2020).

32. Z. Rao, Y. Lu, Z. Li, K. Sim, Z. Ma, J. Xiao, C. Yu, Curvy, shape-adaptive imagers based on printed optoelectronic pixels with a kirigami design. *Nat. Electron.* **4**, 513–521 (2021).
33. M. Mahmood, S. Kwon, H. Kim, Y.-S. Kim, P. Siriaraya, J. Choi, B. Otkhmezuri, K. Kang, K. J. Yu, Y. C. Jang, C. S. Ang, W.-H. Yeo, Wireless soft scalp electronics and virtual reality system for motor imagery-based brain–machine interfaces. *Adv. Sci.* **2021**, 2101129 (2021).
34. X. Yu, Z. Xie, Y. Yu, J. Lee, A. Vazquez-Guardado, H. Luan, J. Ruban, X. Ning, A. Akhtar, D. Li, B. Ji, Y. Liu, R. Sun, J. Cao, Q. Huo, Y. Zhong, C. Lee, S. Kim, P. Gutruf, C. Zhang, Y. Xue, Q. Guo, A. Chempakasseril, P. Tian, W. Lu, J. Jeong, Y. Yu, J. Cornman, C. Tan, B. Kim, K. Lee, X. Feng, Y. Huang, J. A. Rogers, Skin-integrated wireless haptic interfaces for virtual and augmented reality. *Nature* **575**, 473–479 (2019).
35. Z. Xue, H. Song, J. A. Rogers, Y. Zhang, Y. Huang, Mechanically-guided structural designs in stretchable inorganic electronics. *Adv. Mater.* **32**, 1902254 (2020).
36. Y. Zhang, F. Zhang, Z. Yan, Q. Ma, X. Li, Y. Huang, J. A. Rogers, Printing, folding and assembly methods for forming 3D mesostructures in advanced materials. *Nat. Rev. Mater.* **2**, 17019 (2017).
37. K. Dae-Hyeong, X. Jianliang, S. Jizhou, H. Yonggang, J. A. Rogers, Stretchable, curvilinear electronics based on inorganic materials. *Adv. Materi.* **22**, 2108–2124 (2010).
38. H. Chen, L. Dejace, S. P. Lacour, Electronic skins for healthcare monitoring and smart prostheses. *Annu. Rev. Control Robot. Autonom. Syst.* **4**, 629–650 (2021).
39. S. P. Lacour, G. Courtine, J. Guck, Materials and technologies for soft implantable neuroprostheses. *Nat. Rev. Mater.* **1**, 16063 (2016).
40. F. Fallegger, G. Schiavone, E. Pirondini, F. B. Wagner, N. Vachicouras, L. Serex, G. Zegarek, A. May, P. Constanthin, M. Palma, M. Khoshnevis, D. Van Roost, B. Yvert, G. Courtine, K. Schaller, J. Bloch, S. P. Lacour, MRI-compatible and conformal electrocorticography grids for translational research. *Sci. Adv.* **8**, 2003761 (2021).
41. Y. Khan, A. E. Ostfeld, C. M. Lochner, A. Pierre, A. C. Arias, Monitoring of vital signs with flexible and wearable medical devices. *Adv. Mater.* **28**, 4373–4395 (2016).
42. C. Wang, C. Linghu, S. Nie, C. Li, Q. Lei, X. Tao, Y. Zeng, Y. Du, S. Zhang, K. Yu, H. Jin, W. Chen, J. Song, Programmable and scalable transfer printing with high reliability and efficiency for flexible inorganic electronics. *Sci. Adv.* **6**, eabb2393 (2020).
43. F. Fallegger, G. Schiavone, S. P. Lacour, Conformable hybrid systems for implantable bioelectronic interfaces. *Adv. Mater.* **32**, 1903904 (2020).
44. Y.-S. Guan, A. Thukral, S. Zhang, K. Sim, X. Wang, Y. Zhang, F. Ershad, Z. Rao, F. Pan, P. Wang, J. Xiao, C. Yu, Air/water interfacial assembled rubbery semiconducting nanofilm for fully rubbery integrated electronics. *Sci. Adv.* **6**, eabb3656 (2020).
45. R. Qazi, A. M. Gomez, D. C. Castro, Z. Zou, J. Y. Sim, Y. Xiong, J. Abdo, C. Y. Kim, A. Anderson, F. Lohner, S.-H. Byun, B. Chul Lee, K.-I. Jang, J. Xiao, M. R. Bruchas, J.-W. Jeong, Wireless optofluidic brain probes for chronic neuropharmacology and photostimulation. *Nat. Biomed. Eng.* **3**, 655–669 (2019).
46. Y. J. Tan, G. J. Susanto, H. P. Anwar Ali, B. C. K. Tee, Progress and roadmap for intelligent self-healing materials in autonomous robotics. *Adv. Mater.* **33**, 2002800 (2021).
47. M. H. Kang, G. J. Lee, J. H. Lee, M. S. Kim, Z. Yan, J.-W. Jeong, K.-I. Jang, Y. M. Song, Outdoor-useable, wireless/battery-free patch-type tissue oximeter with radiative cooling. *Adv. Sci.* **8**, 2004885 (2021).
48. A. Petritz, E. Karner-Petritz, T. Uemura, P. Schäffner, T. Araki, B. Stadlober, T. Sekitani, Imperceptible energy harvesting device and biomedical sensor based on ultraflexible ferroelectric transducers and organic diodes. *Nat. Commun.* **12**, 2399 (2021).
49. D.-H. Kim, J. Song, W. M. Choi, H.-S. Kim, R.-H. Kim, Z. Liu, Y. Y. Huang, K.-C. Hwang, Y.-w. Zhang, J. A. Rogers, Materials and noncoplanar mesh designs for integrated circuits with linear elastic responses to extreme mechanical deformations. *Proc. Natl. Acad. Sci.* **105**, 18675–18680 (2008).
50. S. Xu, Y. Zhang, J. Cho, J. Lee, X. Huang, L. Jia, J. A. Fan, Y. Su, J. Su, H. Zhang, H. Cheng, B. Lu, C. Yu, C. Chuang, T.-i. Kim, T. Song, K. Shigeta, S. Kang, C. Dagdeviren, I. Petrov, P. V. Braun, Y. Huang, U. Paik, J. A. Rogers, Stretchable batteries with self-similar serpentine interconnects and integrated wireless recharging systems. *Nat. Commun.* **4**, 1543 (2013).
51. S. Xu, Y. Zhang, L. Jia, K. E. Mathewson, K.-I. Jang, J. Kim, H. Fu, X. Huang, P. Chava, R. Wang, S. Bhole, L. Wang, Y. J. Na, Y. Guan, M. Flavin, Z. Han, Y. Huang, J. A. Rogers, Soft microfluidic assemblies of sensors, circuits, and radios for the skin. *Science* **344**, 70–74 (2014).
52. Y. Zhang, S. Wang, X. Li, J. A. Fan, S. Xu, Y. M. Song, K.-J. Choi, W.-H. Yeo, W. Lee, S. N. Nazaar, B. Lu, L. Yin, K.-C. Hwang, J. A. Rogers, Y. Huang, Experimental and theoretical studies of serpentine microstructures bonded to prestrained elastomers for stretchable electronics. *Adv. Funct. Mater.* **24**, 2028–2037 (2014).
53. K.-I. Jang, K. Li, H. U. Chung, S. Xu, H. N. Jung, Y. Yang, J. W. Kwak, H. H. Jung, J. Song, C. Yang, A. Wang, Z. Liu, J. Y. Lee, B. H. Kim, J.-H. Kim, J. Lee, Y. Yu, B. J. Kim, H. Jang, K. J. Yu, J. Kim, J. W. Lee, J.-W. Jeong, Y. M. Song, Y. Huang, Y. Zhang, J. A. Rogers, Self-assembled three dimensional network designs for soft electronics. *Nat. Commun.* **8**, 15894 (2017).
54. Z. Yang, Z. Zhai, Z. Song, Y. Wu, J. Liang, Y. Shan, J. Zheng, H. Liang, H. Jiang, Conductive and elastic 3D helical fibers for use in washable and wearable electronics. *Adv. Mater.* **32**, 1907495 (2020).
55. A. Mamidanna, Z. Song, C. Lv, C. S. Lefky, H. Jiang, O. J. Hildreth, Printing stretchable spiral interconnects using reactive ink chemistries. *ACS Appl. Mater. Inter.* **8**, 12594–12598 (2016).
56. S. Heo, J. Ha, S. J. Son, I. S. Choi, H. Lee, S. Oh, J. Jekal, M. H. Kang, G. J. Lee, H. H. Jung, J. Yea, T. Lee, Y. Lee, J.-W. Choi, S. Xu, J. H. Choi, J.-W. Jeong, Y. M. Song, J.-C. Rah, H. Keum, K.-I. Jang, Instant, multiscale dry transfer printing by atomic diffusion control at heterogeneous interfaces. *Sci. Adv.* **7**, eabh0040 (2021).
57. C. Y. Kim, M. J. Ku, R. Qazi, H. J. Nam, J. W. Park, K. S. Nam, S. Oh, I. Kang, J.-H. Jang, W. Y. Kim, J.-H. Kim, J.-W. Jeong, Soft subdermal implant capable of wireless battery charging and programmable controls for applications in optogenetics. *Nat. Commun.* **12**, 535 (2021).
58. N. Rodeheaver, R. Herbert, Y.-S. Kim, M. Mahmood, H. Kim, J.-W. Jeong, W.-H. Yeo, Strain-isolating materials and interfacial physics for soft wearable bioelectronics and wireless, motion artifact-controlled health monitoring. *Adv. Funct. Mater.* **2021**, 2104070 (2021).
59. Y. Yang, Y. Song, X. Bo, J. Min, O. S. Pak, L. Zhu, M. Wang, J. Tu, A. Kogan, H. Zhang, T. K. Hsiai, Z. Li, W. Gao, A laser-engraved wearable sensor for sensitive detection of uric acid and tyrosine in sweat. *Nat. Biotechnol.* **38**, 217–224 (2020).
60. Y. Song, J. Min, Y. Yu, H. Wang, Y. Yang, H. Zhang, W. Gao, Wireless battery-free wearable sweat sensor powered by human motion. *Sci. Adv.* **6**, eaay9842 (2020).
61. T. Araki, L. M. Bongartz, T. Kaiju, A. Takemoto, S. Tsuruta, T. Uemura, T. Sekitani, Flexible neural interfaces for brain implants-the pursuit of thinness and high density. *Flex. Print. Electron.* **5**, 043002 (2020).
62. J. W. Lee, R. Xu, S. Lee, K.-I. Jang, Y. Yang, A. Banks, K. J. Yu, J. Kim, S. Xu, S. Ma, S. W. Jang, P. Won, Y. Li, B. H. Kim, J. Y. Choe, S. Huh, Y. H. Kwon, Y. Huang, U. Paik, J. A. Rogers, Soft, thin skin-mounted power management systems and their use in wireless thermography. *Proc. Natl. Acad. Sci.* **113**, 6131–6136 (2016).
63. Z. Huang, Y. Hao, Y. Li, H. Hu, C. Wang, A. Nomoto, T. Pan, Y. Gu, Y. Chen, T. Zhang, W. Li, Y. Lei, N. Kim, C. Wang, L. Zhang, J. W. Ward, A. Maralani, X. Li, M. F. Durstock, A. Pisano, Y. Lin, S. Xu, Three-dimensional integrated stretchable electronics. *Nat. Electron.* **1**, 473–480 (2018).
64. K.-I. Jang, H. U. Chung, S. Xu, C. H. Lee, H. Luan, J. Jeong, H. Cheng, G.-T. Kim, S. Y. Han, J. W. Lee, J. Kim, M. Cho, F. Miao, Y. Yang, H. N. Jung, M. Flavin, H. Liu, G. W. Kong, K. J. Yu, S. I. Rhee, J. Chung, B. Kim, J. W. Kwak, M. H. Yun, J. Y. Kim, Y. M. Song, U. Paik, Y. Zhang, Y. Huang, J. A. Rogers, Soft network composite materials with deterministic and bio-inspired designs. *Nat. Commun.* **6**, 6566 (2015).
65. Q. Ma, H. Cheng, K.-I. Jang, H. Luan, K.-C. Hwang, J. A. Rogers, Y. Huang, Y. Zhang, A nonlinear mechanics model of bio-inspired hierarchical lattice materials consisting of horseshoe microstructures. *J. Mech. Phys. Solids* **90**, 179–202 (2016).
66. H. Zhang, X. Guo, J. Wu, D. Fang, Y. Zhang, Soft mechanical metamaterials with unusual swelling behavior and tunable stress-strain curves. *Sci. Adv.* **4**, eaar8535 (2018).
67. D. Yan, J. Chang, H. Zhang, J. Liu, H. Song, Z. Xue, F. Zhang, Y. Zhang, Soft three-dimensional network materials with rational bio-mimetic designs. *Nat. Commun.* **11**, 1180 (2020).
68. J. Liu, D. Yan, W. Pang, Y. Zhang, Design, fabrication and applications of soft network materials. *Mater. Today* **49**, 324–350 (2021).
69. J. Liu, D. Yan, Y. Zhang, Mechanics of unusual soft network materials with rotatable structural nodes. *J. Mech. Phys. Solids* **146**, 104210 (2021).
70. R. Lin, H.-J. Kim, S. Achavananthadith, S. A. Kurt, S. C. C. Tan, H. Yao, B. C. K. Tee, J. K. W. Lee, J. S. Ho, Wireless battery-free body sensor networks using near-field-enabled clothing. *Nat. Commun.* **11**, 444 (2020).
71. T. Pan, M. Pharr, Y. Ma, R. Ning, Z. Yan, R. Xu, X. Feng, Y. Huang, J. A. Rogers, Experimental and theoretical studies of serpentine interconnects on ultrathin elastomers for stretchable electronics. *Adv. Funct. Mater.* **27**, 1702589 (2017).
72. Y. Zhang, S. Xu, H. Fu, J. Lee, J. Su, K.-C. Hwang, J. A. Rogers, Y. Huang, Buckling in serpentine microstructures and applications in elastomer-supported ultra-stretchable electronics with high areal coverage. *Soft Matter* **9**, 8062–8070 (2013).
73. H. U. Chung, B. H. Kim, J. Y. Lee, J. Lee, Z. Xie, E. M. Ibler, K. Lee, A. Banks, J. Y. Jeong, J. Kim, C. Ogle, D. Grande, Y. Yu, H. Jang, P. Assem, D. Ryu, J. W. Kwak, M. Namkoong, J. B. Park, Y. Lee, D. H. Kim, A. Ryu, J. Jeong, K. You, B. Ji, Z. Liu, Q. Huo, X. Feng, Y. Deng, Y. Xu, K.-I. Jang, J. Kim, Y. Zhang, R. Ghaffari, C. M. Rand, M. Schau, A. Hamvas, D. E. Weese-Mayer, Y. Huang, S. M. Lee, C. H. Lee, N. R. Shanbhag, A. S. Paller, S. Xu, J. A. Rogers, Binodal, wireless epidermal electronic systems with in-sensor analytics for neonatal intensive care. *Science* **363**, eaau0780 (2019).
74. D.-H. Kim, N. Lu, R. Ma, Y.-S. Kim, R.-H. Kim, S. Wang, J. Wu, S. M. Won, H. Tao, A. Islam, K. J. Yu, T.-i. Kim, R. Chowdhury, M. Ying, L. Xu, M. Li, H.-J. Chung, H. Keum, M. McCormick, P. Liu, Y.-W. Zhang, F. G. Omenetto, Y. Huang, T. Coleman, J. A. Rogers, Epidermal electronics. *Science* **333**, 838–843 (2011).

75. H. Kim, Y.-S. Kim, M. Mahmood, S. Kwon, N. Zavanelli, H. S. Kim, Y. S. Rim, F. Epps, W.-H. Yeo, Fully integrated, stretchable, wireless skin-conformal bioelectronics for continuous stress monitoring in daily life. *Adv. Sci.* **7**, 2000810 (2020).
76. S. Han, J. Kim, S. M. Won, Y. Ma, D. Kang, Z. Xie, K.-T. Lee, H. U. Chung, A. Banks, S. Min, S. Y. Heo, C. R. Davies, J. W. Lee, C.-H. Lee, B. H. Kim, K. Li, Y. Zhou, C. Wei, X. Feng, Y. Huang, J. A. Rogers, Battery-free, wireless sensors for full-body pressure and temperature mapping. *Sci. Trans. Med.* **10**, eaan4950 (2018).

Acknowledgments: We thank X. Feng from the Tsinghua University for offering access to microfabrication facilities in the laboratory and Q. Li from the Tsinghua University for assistance in peeling test. **Funding:** Y.Z. acknowledges support from the National Natural Science Foundation of China (grant nos. 12050004 and 11921002), the Tsinghua National Laboratory for Information Science and Technology, and a grant from the Institute for Guo Qiang, Tsinghua University (grant no. 2019GQG1012). H.S. acknowledges support from National Natural Science Foundation of China (grant no. 11902178), Natural Science Foundation of Beijing Municipality (grant no. 3204043), China Postdoctoral Science Foundation (grant no. 2019M650648), and Opening Project of the Key Laboratory of Bionic Engineering (Ministry of Education), Jilin University (no. K201901). Z.X. acknowledges support from National Natural Science Foundation of China (grant no. 61904095). **Author contributions:** Y.Z. designed and supervised the research. Y.Z., H.S., and G.L. led the structural designs, mechanics modeling, and experimental work, with assistance from Z.J., R.B., Z.X., and D.Y. H.S. led the fabrication and experimental characterization of the encapsulated serpentine interconnects and the stretchable electronic system, with the assistance from F.Z., K.B., J.L., X.C., W.P., and Z.S. Y.Z., H.S., and G.L. wrote the manuscript and designed the figures. All authors commented on the paper. **Competing interests:** The authors declare that they have no competing interests. **Data and materials availability:** All data needed to evaluate the conclusions in the paper are present in the paper and/or the Supplementary Materials.

Submitted 14 September 2021
Accepted 24 January 2022
Published 16 March 2022
10.1126/sciadv.abm3785